The correlation of electronic properties with nanoscale morphological variations measured by SPM on semiconductor devices

2003 J. Phys.: Condens. Matter 15 S3095

(http://iopscience.iop.org/0953-8984/15/42/008)

INSTITUTE OF PHYSICS PUBLISHING JOURNAL OF PHYSICS: CONDENSED MATTER

J. Phys.: Condens. Matter **15** (2003) S3095–S3112 PII: S0953-8984(03)66052-2

The correlation of electronic properties with nanoscale morphological variations measured by SPM on semiconductor devices

P R Dunstan, T G G Maffeïs, M P Ackland, G T Owen and S P Wilks

Multidisciplinary Nanotechnology Centre, Faraday Tower, University of Wales Swansea, Singleton Park, Swansea SA2 8PP, UK

Received 14 July 2003
Published 10 October 2003
Online at stacks.iop.org/JPhysCM/15/S3095

Abstract

In this paper we present two examples of how scanning probe microscopy (SPM) techniques can be used to correlate the electronic properties with the surface topography of electronic devices down to the nanometre range. There is an increasing need for such techniques as the size of devices shrinks continually and therefore nanometre-sized features become more important. To illustrate the usefulness of SPM we first focus on scanning tunnelling microscopy/scanning tunnelling spectroscopy (STM–STS) studies of sintered nanocrystalline gas sensors made from 8 nm SnO_2 nano-powder. Analysis of simultaneously acquired STS measurements and STM topography show that the apparent surface band gap measured by STS was significantly narrower at nanoparticles' boundaries than at centres. Changes in the conduction band edge position were much more pronounced than for the valence band and are mostly responsible for the variation in band gap. The preferential chemisorption of oxygen species at sintering necks causing an increase in surface state density has been put forward as a possible interpretation. The second example shows how a modified scanning near-field optical microscope (SNOM) can be used to simultaneously acquire topographic and photocurrent maps of Ni–SiC Schottky diodes. The photocurrent was generated by illuminating with laser light emitted through the nanometre sized SNOM aperture, thus locally exciting electrons over the Schottky barrier. By comparing the photocurrent and topography maps it is therefore possible to detect, with submicron resolution, changes in the local electronic properties of the interface. We have shown that annealing the Ni contacts produces clustering on the surface and an increase in the Schottky barrier height. Local measurements of the photocurrent were mapped simultaneously with the topography and the possibility of artefacts discussed. The photocurrent map of annealed contacts indicated a switching behaviour and the generation of voids within the Ni surface/interface has been proposed as a probable mechanism for this effect.

1. Introduction

The correlation between structure and electronic properties has been used to tailor material characteristics for many years and has led to significant progress in the development of semiconductor device technology. The understanding of surface and interface physics has been vital in this development and has given rise to low dimensional systems which exploit quantum mechanical properties and electron confinement. More recently the development of 2d and 1d systems has led to further technological breakthroughs. However it is clear that fundamental issues related to structural, chemical, electrical and optical properties on the nanoscale are crucial to the continued expansion of technology. For example, morphological variations on the nanoscale can range from single atoms to large atomic clusters and their impact on device characteristics can be significant. In this paper we address two devices whose operation depends hugely on morphological variations at the nanoscale related to both surfaces and interfaces, namely nanocrystalline gas sensors and Schottky contacts respectively. Nanocrystalline gas sensors rely on the interaction between a target gas and surface particles, leading to a change in electronic properties of the sensor. However, the effective *surface* mechanism is unclear and the efficiency of their operation remains an important area of development. Metal contacts to semiconductors have been a hugely important and an active area of research for a number of decades, the field still remaining in focus as dimensions have shrunk and new material systems explored. The stability of *interface* properties helps to ensure reproducible Schottky barrier heights and device characteristics; moreover, tailoring these properties allows for optimisation of device operation. It is clear that in both examples, nanoscale issues dictate the mechanisms governing the electrical properties of each device. Hence by using scanning probe microscopy (SPM) techniques to extract properties at the nanoscale, which can be directly correlated with morphology in the same spatial regime, the fundamental aspects of such devices can be understood and hence tailored. These are the issues that this paper addresses.

2. Background

In order to understand the nanoscale morphological issues that dictate the electrical characteristics of the device, it is important to have a basic understanding of the issues related to each device that will be discussed in this paper. Hence the following section provides some background related to the operation and nanoscale morphological features that are believed to dictate device behaviour.

Nanocrystalline SnO_2 gas sensors. Gas sensors based on polycrystalline SnO_2 offer many advantages over current technologies for detecting reducing gases, such as low cost, long lifetime and high selectivity and sensitivity. The sensing mechanism relies on perturbations in surface conductivity induced by chemical reactions between reducing target gases and oxygen species chemisorbed onto the SnO_2 particles [1, 2]. The net effect observed is a variation in the bulk resistance of the polycrystalline sensing film. Chemisorbed oxygen species from the air act as electron acceptors, increasing the overall resistance. When reducing gas molecules react with the chemisorbed oxygen, electrons are returned to the SnO_2 and the resistance decreases. Gas sensing devices operate at temperatures in the 100–400 °C range to promote chemical reactions. In order to maximise the specific area (surface to volume ratio) and therefore the sensitivity (ratio of the resistance before and during exposure to target gases), SnO_2 gas sensors usually consist of porous films made up of SnO_2 particles with diameters in the nanometre range. The properties of nanoscale features therefore dictate the gas sensing

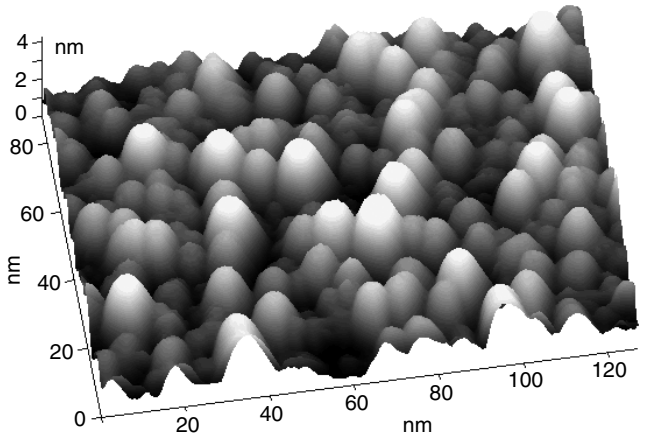

Figure 1. Constant current STM image of 8 nm SnO_2 particles (deposited on silicon) acquired at a sample bias of −3 V, tunnelling setpoint of 0.3 nA and at a sample temperature of 100 °C.

mechanism. Yet the sensing mechanism at the molecular level is not fully understood, which hinders SnO_2 based sensing devices from realizing their full potential. More details on the gas sensing properties of nanoscale semiconducting oxide powders can be found in [3]. Scanning tunnelling microscopy/scanning tunnelling spectroscopy (STM–STS), with its unique ability to correlate electronic and topographical information at the atomic level, is an ideal technique to investigate the interaction of nanoparticles with gas molecules at elevated temperature. Figure 1 shows an STM image of SnO_2 nanoparticles deposited on silicon acquired at elevated temperature, clearly resolving 8 nm SnO_2 particles. In this paper we focus on the crucial issue of sintering of 8 nm particles, using STM–STS to correlate the surface electronic properties of the sintered nanoparticles with the local morphology.

Schottky barrier heights on Ni–SiC contacts. The intrinsic properties of silicon carbide, namely its wide band gap (3.3 eV for 4H-polytype), high thermal conductivity and high critical electric field, provide an ideal platform for the next generation of semiconductor devices. As a result SiC represents an area of great technological interest due to future applications in high power and high operational temperature environments. Many issues associated with bulk properties and defects have been overcome and the limiting factors are now associated with SiC interfaces, in particular Schottky and Ohmic contacts. Variations in Schottky diode performance due to the contact properties on the nanoscale remain an area which needs further development and characterization. These interface issues arise due to the reactive nature of the SiC material and its tendency to dissociate when in intimate contact with other materials at high temperatures. Transmission electron microscopy (TEM) measurements have indicated reactions at high temperature and the generation of voids [4]. It is generally accepted that these degrade the electrical properties and reliability of the contact. The use of surface passivating layers [5] and controlled interlayers offers options for further improvement of interface stability and inhibiting interface reactions, but techniques which can monitor these effects are vital. The use of a scanning near-field optical microscope (SNOM) to probe the interface between two materials has been carried out by a number of groups [6–8] and we have sought to develop this for monitoring changes in Schottky barrier height for the Ni–SiC system. Samples were produced for these measurements with different barrier heights and the aim was to see if the localised photocurrents mapped by the SNOM based technique would indicate the homogeneity of the contact in relation to its production.

3. Scanning probe microscopy techniques

Methods that allow characterization of structures on a nanometre scale are of vital importance, and as the physical dimensions of devices shrink further, the surface/interface properties grow in their significance. SPM techniques have revolutionised the way in which research can be undertaken at such spatial distributions, and the developments in this field have in many ways led to swift advances in device based technologies. In particular, STM has permitted surfaces of materials to be imaged on an atomic scale and has also been used in cross section to study device physics directly. Many SPM related imaging techniques can give additional information and are not just limited to topography. For example, localised current–voltage (I–V) measurements made during an STM image (STS) can reveal the electronic density of states correlated simultaneously with the topographic structure. Similarly in atomic force microscopy, picoNewton forces or adhesion can be associated with structural features. Combining all elements of the SPM techniques it is possible to clearly correlate physical information with topographic features, for example the electronic properties of atomic defects on the surface of a cleaved laser facet [9]. In this paper we concentrate on two SPM techniques which are distinctly different in their mode of operation and imaging mechanism, which can yield electronic characteristics at surfaces and at interfaces.

3.1. Scanning tunnelling microscopy (STM) and spectroscopy (STS)

STM is well known for its morphological capabilities within the atomic regime when examining conducting surfaces. A detailed description of the STM technique will not be given here as it has been addressed by others [10], although a schematic figure is shown in figure 2. However, it is worth commenting on the care required when interpreting images as STM experiments produce a map of the electron density across a surface which is therefore a mixture of both topography and local electronic effects. Hence it is clear that care must be taken when inferring structural information. This issue can become even more important when delocalisation occurs in the bonding at the surface, as a correlation between atomic positions and regions of high charge density is difficult to infer. Under such conditions, the electronic information must be decoupled from the topography using a combination of bias dependent imaging and theoretical modelling. To complicate the matter further, the nature of the STM tip is also important. For example, even if the tip is atomically sharp permitting the maximum spatial resolution, features in the image, and also the image contrast, can be dependent on the presence of contaminants or adsorbates at the tip apex. The finite size of the tip apex (radius of curvature) can also influence the STM images. Therefore, when using the STM technique, the operator must be aware of these issues when interpreting the results and hence experimental vigilance and reproducibility are paramount.

If one assumes that the image can be successfully characterized and understood in terms of the local surface structure using STM, STS can be applied to probe the corresponding local electronic properties [11]. STS is still in its infancy compared to STM, as it requires ultimate stability between the sample and the tip for the measurements to be meaningful. The technique is based on performing local I–V measurements as the image is simultaneously acquired. In theory, this means that the local electronic properties can be directly correlated with the structural features on the surface. An example of an I–V characteristic, taken from a SnO_2 surface, is shown in figure 3(a) where two regions of conductivity can be seen, either side of an area of non-conductivity. The former regions are associated with current derived from valence and conduction band states probed under negative and positive sample bias respectively, whilst the region of non-conductivity corresponds to the band gap. The Fermi level is located at zero bias when natural equilibrium occurs. Feenstra *et al* [12] demonstrated that when such an I–V

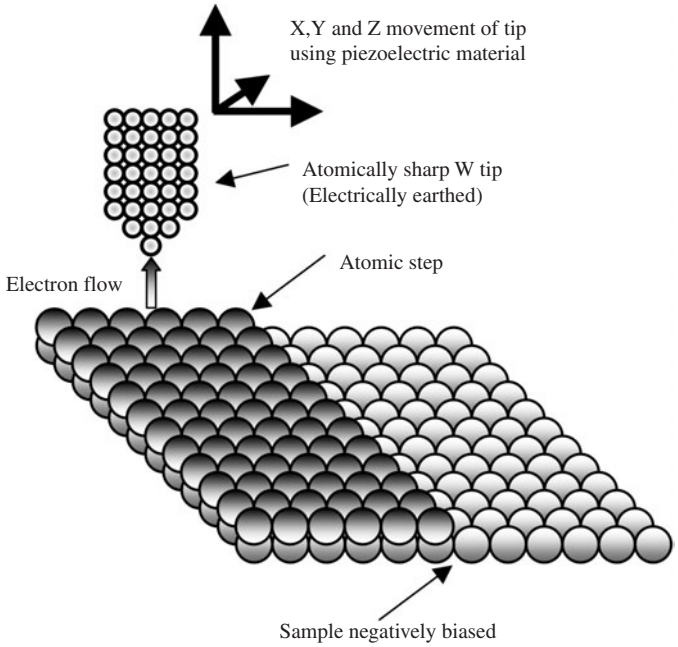

Figure 2. Schematic of a typical planar STM set-up where the tip operates in a constant current mode. The tip will follow the undulations in surface charge to maintain the current by moving closer to or further away from the sample surface to provide a topographic image. The negative sample bias causes electrons to flow from the sample to the tip. Hence the tip is probing the full valence band sates of the sample.

curve is converted to a differential conductivity, which is normalized with respect to I/V, as a function of sample bias, a measure of the effective density of states across the band edges and gap region can be observed. This is also shown in figure 3(b). The Fermi level is located at mid-gap due to the transfer of charge from the SnO_2 to chemisorbed oxygen species, and not at the conduction band edge as one might expect for an n-type semiconductor. Again, care must be taken when interpreting such data as several assumption are made regarding the nature of the sample–tip interaction:

(a) the tip field does not induce band bending within the sample,
(b) the tip is a single source which is atomically sharp, and
(c) the density of states in the tip around the Fermi level is constant.

The use of highly doped samples can counteract the effect of tip induced band bending whilst effects derived from the nature of the tip are often evident from the quality and reproducibility of the STM image. Additionally, comparing curves acquired at different tip–sample distances (different tunnelling conditions) can help in the interpretation of STS data.

Since the STS technique yields the position of the conduction and valence band edges relative to the Fermi level, it can be used to reveal band bending, bandgap and band features as a function of topography. This is normally achieved using STM and STS simultaneously where the local electronic properties can be correlated with structural features extracted from the STM image.

3.2. Scanning near-field optical microscopy (SNOM)

One of the more recent SPM developments has implemented an optical light source on the nanoscale, capable of overcoming the conventional diffraction limit of $\sim\lambda/2$. Although

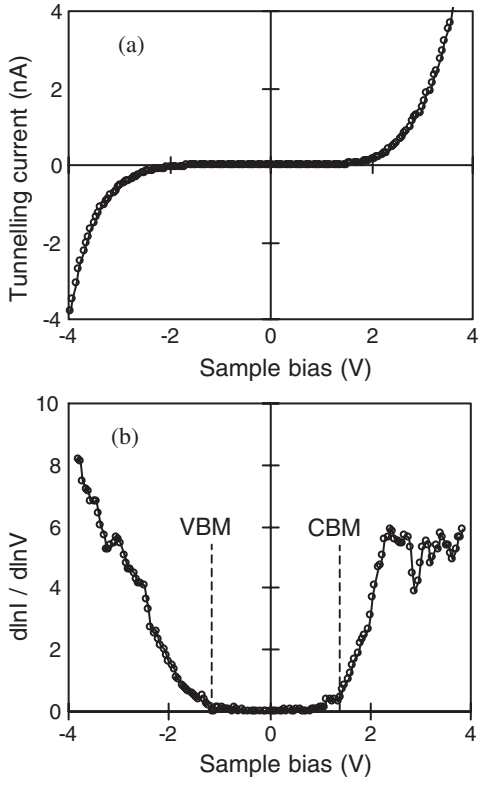

Figure 3. (a) Tunnelling current and (b) normalized conductivity versus sample bias for nanocrystalline SnO_2. The positions of the VBM and CBM are shown by vertical dashed lines. The Fermi level (zero bias) is located at mid-gap, indicating surface band bending caused by chemisorbed oxygen.

technically realized in the early 1980s [13], the idea was originally proposed by Synge in 1928 [14]. The technique is known as scanning near-field optical microscopy (SNOM) and in its most common configuration, the aperture-SNOM, comprises a metal-clad tapered optical fibre with a sub-wavelength aperture at the apex, serving as a localized light source. Raster scanning of the optical probe along a sample's surface, at a constant gap (less than the diameter of the aperture), and the simultaneous collection of scattered light in the far-field for each probe position, results in optical image generation of sub-λ resolution. The SNOM probe–sample distance is regulated by the use of the shear-force feedback mechanism of a quartz tuning fork [15], holding the SNOM aperture in close proximity to the sample surface, in the near-field regime. The light at the aperture has a near-field component which decays exponentially away from the aperture. If the sample is very close to the aperture this near-field component can also be coupled into the surface and made to propagate, leading to a greatly increased signal which is extremely sensitive to aperture–sample distance. This arrangement can dramatically alter the optical resolution obtained, as image resolution is dictated by the size of the tip aperture rather than the wavelength of the light used. Many authors and books have addressed the full details of this technique and its theoretical description, and the reader is directed to those studies [16, 17]. SNOM has recently been exploited on many material systems from semiconductors to biological based samples. For example, the localised nature of the light has been exploited to make submicron optical measurements on fluorescently tagged molecules [18], and also used to promote charge carriers within semiconductor materials [19–21]. The ability of the technique to take advantage of optical spectroscopy on a nanoscale has exciting implications for the development of the technique, although many problems related

to the near-field do complicate further advances. The super resolution capability of SNOM relies on the strong coupling of the near-field light from the probe aperture. This makes the tip–sample separation and control paramount in the application of the technique because fluctuations can lead to direct correlation between topography and optical response even when there is no variation in refractive index on the sample surface. The production of artefacts within the optical response as a function of topography can be related to the feedback control of the probe and thus the effect reduced by careful attention to scanning parameters. This has been addressed by several authors [22, 23] who have focussed on constant gap control and detailed analysis of images in which anti-correlation between topography and optical response is sought. These factors have been taken into account in our studies, as the topography of the samples is not atomically flat. Monitoring the optical response as a function of scan parameter has indicated the optimum settings to minimize artefact generation, and these have then been implemented for photocurrent measurements.

SNOM has been previously used in a technique analogous to optical beam induced currents to promote charge carriers across metal–semiconductor barriers [24]. Using the near-field light it is possible to map the excitation and resulting current response in the sample, thus probing the interface barrier properties on the nanoscale. The technique is similar in many ways to ballistic electron emission microscopy/spectroscopy [25, 26], in which the metal STM tip injects electrons into a metal contact and ballistic electrons (those with an energy greater than the Schottky barrier) are detected in the semiconductor. Coluzza *et al* [24] indicated the power of the SNOM based technique using a tuneable laser source to locally map the variation of the Schottky barrier height across a surface/interface.

4. Results

4.1. SnO_2 gas sensors

4.1.1. Sintering of SnO_2 nanoparticles. SnO_2 gas sensing films fabricated with nanopowders or clusters are sometimes annealed in air (sintered) after deposition in order to promote the formation of sintering necks between adjacent particles. These sintering necks and their morphology alter the sensing mechanism dramatically [27, 28] but the optimum anneal conditions (temperature, duration) can only be determined by indirect methods such as conductivity measurements. STM and STS can provide a direct observation of the sintering process on a nanometre scale, which can be correlated with electronic properties of the sensor surface over the same spatial regime.

In the absence of sintering, electrons flowing between adjacent, touching nanocrystals must overcome a barrier potential at the boundaries similar to that of a Schottky barrier at a metal–semiconductor interface. The height of the potential barrier is modified by the transfer of charges between the surface of the sensor and adsorbed gases. The current flow between nanocrystals depends exponentially on this potential barrier, which explains the high sensitivity of the sensors. When the SnO_2 particles have been sintered, electrons can flow from one nanocrystal to the next more easily through sintering necks, and the total resistance of the sensor is lowered. In this case the sensitivity to target gases arises from the control of current flow in the necks, in much the same way as the gate voltage controls current flow in the channel of a field-effect transistor. The adsorption of oxidizing gases results in a depletion layer extending into the necks, thus restricting current flow. Conversely, reducing gases lead to an increase in conductivity. The sensitivity of the sensor is thus determined by the size of the sintering necks compared to the depletion layer depth, given by the Debye length of electrons, typically 1–5 nm, depending on the bulk electron concentration. If the sintering necks are about the same size as the Debye length, then they can become fully depleted in the

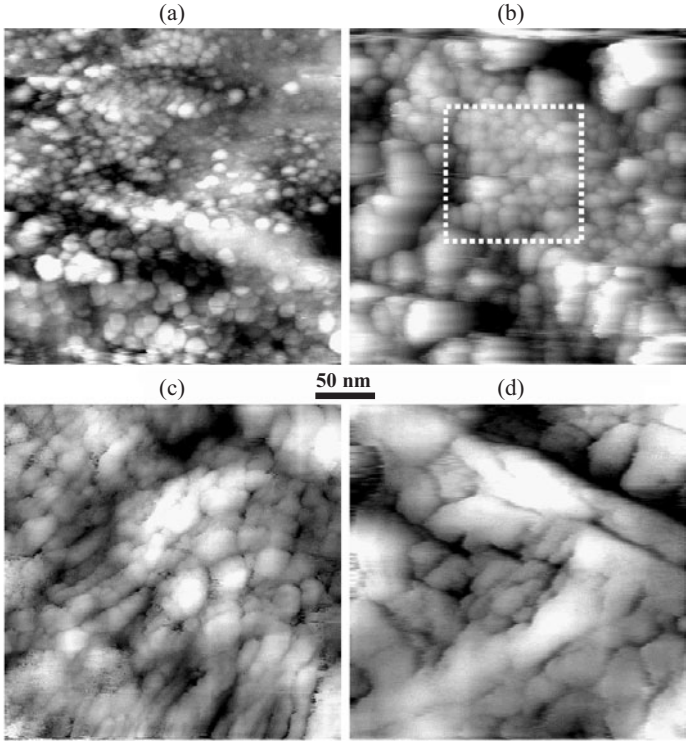

Figure 4. 250 × 250 nm^2 STM constant current images of four SnO_2 films annealed at (a) 400 °C for 20 min, (b) 450 °C for 20 min, (c) 450 °C for 60 min, (d) 500 °C for 60 min. The grey scales represent a topographic height of 5.8, 11.2, 4.1 and 6.6 nm, respectively. The image shows the changes in topography as the nanoparticles merge together.

presence of oxidizing gases, thus resulting in large variations of the conductivity. However, understanding how the degree of sintering dictates the change in conductivity is crucial to the optimization of the device itself.

The samples used in this study were prepared by depositing droplets of a dispersion of SnO_2 nano-powder onto polished silicon substrates. The powder was produced by laser ablation of a ceramic rod. The fabrication details are published elsewhere [29]. TEM and x-ray diffraction analysis of the powder showed that the particles were monocrystalline, roughly spherical with a distribution of diameters centred around 8 nm. After drying on a hot plate to evaporate the dispersion liquid (alpha-turpineol), four samples were annealed in air under four different conditions: 400 °C for 20 min, 450 °C for 20 min, 450 °C for 60 min and 500 °C for 60 min. After sintering, the samples were then loaded into an ultra high vacuum (UHV) STM system (base pressure of 10^{-11} mbar) and scanned at room temperature using an electrochemically etched W tip.

Figure 4 shows a large-scale image for each of the annealed samples. Densely packed individual spherical particles can clearly be seen on the sample annealed at 400 °C for 20 min (figure 4(a)). The size of the nanoparticles ranges from 6 to 12 nm, in good agreement with the powder specifications. This result has been repeatedly confirmed with different W tips and also using cut Pt/Ir tips on a different STM system in air. Figure 4(b) shows an image from a sample fabricated under the same conditions, but annealed at 450 °C for 20 min. Individual particles of size 8–15 nm can again be observed, as was the case for the previous image. However, the nanoparticles are more closely packed and seem to be losing their spherical shape. It could

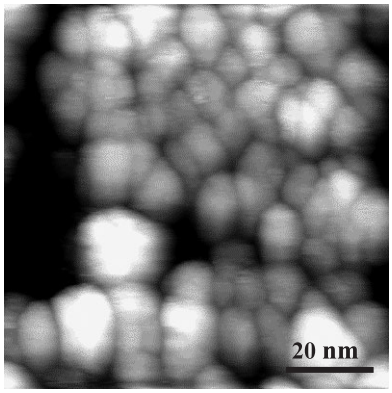

Figure 5. 100×100 nm^2 STM constant current image of an SnO_2 film annealed at 450 °C for 20 min (zoom of image (b) on figure 4). The grey scale range is 0–9.2 nm. The nanoparticles start to lose their spherical shape and arrange themselves in a tiling pattern.

be that the nanoparticles have started to merge as a result of the higher temperature anneal. This is more apparent on the close-up view in figure 5, where the nanoparticles appear to have arranged themselves in a tiling pattern. The fact that the size of the nanoparticles is, on average, greater than for the previous annealing conditions suggests that the smallest particles ($<$8 nm) might have completely merged to form larger clusters. This indicates that the sintering process occurs at temperatures below 450 °C. Figure 4(c), taken from the sample annealed at 450 °C for 60 min, indicates that the duration of the anneal is also a significant parameter, as individual grains cannot be observed. The image shows larger regions without defined shapes, probably produced by the merging of the spherical nanoparticles. This trend is confirmed by the last image (figure 4(d)), taken from the sample annealed at 500 °C for 60 min. In this image, the large, shapeless regions have increased in size as the merging process continues. Again these topographies have been checked using different tips. It is however crucial for the sensor performance that merging of the nanoparticles should be avoided during the sintering anneal.

This study suggests that sintering can be interpreted as the beginning of the merging process and that the last three annealing conditions (450 °C for 20 min, 450 °C for 60 min and 500 °C for 60 min) have gone beyond sintering. Figure 6 shows a planar and three-dimensional close-up view of a sample made with 0.6% (in weight) added Sb in order to increase the conductivity of the film, and annealed at 400 °C for 20 min. This sample was in addition outgassed in UHV at about 200 °C for 1 h. The 3D view seems to show some degree of merging between adjacent nanoparticles. The top-right line profile (a) shows that the centres of the two 8 nm particles are about 5 nm apart, leading to the formation of a sintering neck about 70% as large as the nanoparticles. The bottom-left line profile (b), on the other hand, shows a much reduced merging, resulting in negligible sintering. The bottom-right profile (c) shows an intermediate case, with a sintering neck about 50% the size of the nanoparticles. The non-uniformity of sintering could be due to the initial arrangement of the nanoparticles, with densely packed particles more likely to sinter. Electrochemically etched W tips typically have a radius of curvature between 5 and 50 nm. However, tunnelling often occurs from 'minitips' at the apex, giving a much higher lateral resolution [30]. We believe this is the case for the results presented in figure 6, as the tip can clearly resolve the 8 nm particles and reach between them when the degree of sintering is small, as shown on the line profile of figure 6(b). It is only when the distance between two nanoparticle centres is shorter than 8 nm (figure 6(a)), i.e. when the particles have merged together, that the tip cannot reach as far down.

The local differences in the degree of sintering clearly indicate that the variation of the total conductivity of the SnO_2 layer with gas adsorption involves the different mechanisms of electron transport between adjacent nanoparticles presented above. Case (a) is an example of

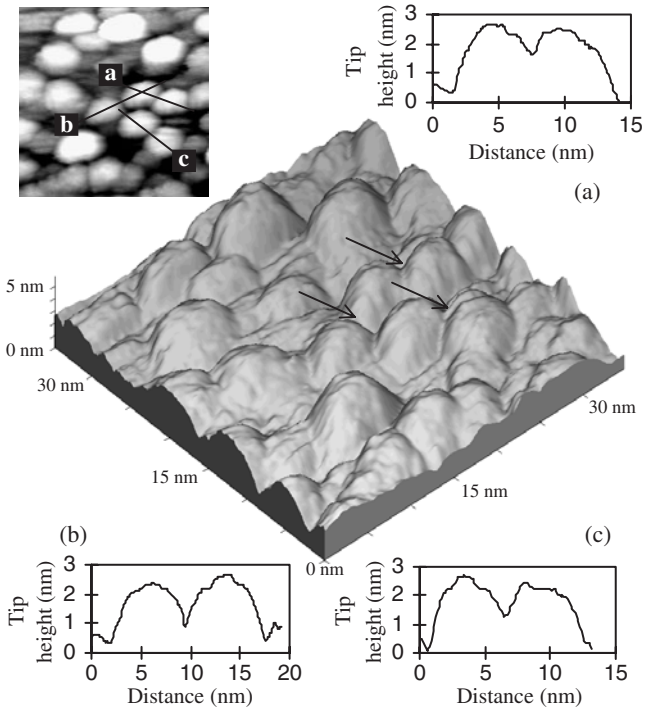

Figure 6. 3D 35 × 35 nm^2 STM constant current image of an SnO_2 sensor annealed at 400 °C for 20 min in air. The arrows indicate the location of various sintering necks. Insets: plane view of the same image, and cross sectional line profiles showing various degrees of sintering.

electron flow controlled by the depth of the depletion layer at the neck; case (b) is equivalent to the 'touching grains' model, in which electrons must overcome a barrier potential at the point of contact; while (c) represent a mixed case, where the small sintering neck might become fully depleted in the presence of oxidizing gases so that electrons must traverse a potential barrier as in (b).

4.1.2. Surface band gap profiling of sintered nanoparticles. Figure 7(a) shows a simultaneously acquired STM–STS image of the same sample as in figure 6, in which the tip stopped scanning every 5 pixels (along the x and y axes) during acquisition of the STM image to record an I–V curve. This grid STS image therefore allows direct correlation of topographical features with surface electronic properties, keeping thermal drift distortion to a minimum. From this image, a set of I–V curves recorded along a line extending across two sintered nanoparticles was analysed with the aim of obtaining a band profile. The numbered (1–17) black and white dots on the image indicate the location of the STS data points used. The average distance between two adjacent dots is 1.1 nm, with an uncertainty of 0.4 nm. In order to extract the position of the valence band maximum (VBM) and conduction band minimum (CBM), the I–V curves were plotted on a semi-log scale with data points below 2 pA discarded as noise. Figure 7(b) shows a selection of such $\log(I)$–V curves. The negative bias current corresponds to electrons tunnelling from the filled valence band states of the SnO_2 nanoparticles into the tip, while positive bias current arises from electrons tunnelling from the tip into the empty conduction band states of the nanoparticles. The position of the band edges was given by the onset of tunnelling at both negative and positive bias. The onsets of tunnelling

did not seem to depend on the tip–sample distance (tunnelling setpoint), although for small current setpoints (below 0.3 nA) the I–V curves were too noisy to adequately determine the onsets. Finally the VBM and CBM are plotted for each STS point, giving the local surface band gap profile of figure 7(c). The band profile reveals wide variations of the surface band gap, from 1 to 4 eV, which can clearly be correlated to the local topography of the nanoparticles. When compared to the tip height profile shown on the same figure, the general trend of the band profile shows that the large band gap values appear to correspond to the centre of the nanoparticles while the small band gap values are found at the edges or boundaries. This trend was repeatedly observed across several nanoparticles. The average band gap over 200 STS points randomly selected is 2.6 eV, while the average band gap over 40 STS points taken from nanoparticle centres only is 2.95 eV.

These values for the surface band gap as measured by STS are much lower than the band gap of bulk single crystal SnO_2 (3.6 eV), but are in good agreement with recent STM results reported by Arbiol *et al* [31], who measured an average band gap of 2.8 eV for nanocrystalline Pd doped SnO_2 printed films (mean crystallite size of 20 nm) in an N_2 atmosphere. This suggests that the surface electronic properties are mostly dominated by surface states, masking the bulk properties. Chemisorbed oxygen species are commonly thought [32] to be the dominant cause of surface states for SnO_2 and are likely to be responsible for the apparent smaller surface band gap (as compared to bulk). However, other impurities such as water vapour, hydrocarbon molecules or the Sb atoms added during preparation, as well as intrinsic states caused by crystalline defects, could also contribute. Additionally, the Fermi level is roughly located at mid-gap, or even closer to the valence band for the large band gaps, despite the fact that SnO_2 is naturally n-doped. This is possibly a consequence of the chemisorbed oxygen removing electrons from the surface and therefore creating a surface barrier.

It is known that STS curves acquired on rough samples might lead to higher current when the tip is positioned over a concave area because of multiple tunnelling paths. However, the fact that the CBM position with respect to the Fermi level varies much more than the VBM seem to indicate that the narrowing of the apparent band gap is not caused by multiple tunnelling paths. Large changes in local electronic properties of polycrystalline material surfaces have been reported before. Kaplan *et al* [33] used STM–STS to characterize vacuum arc deposited amorphous SnO_2 films. They reported I–V curves (taken from different locations on the same film) showing a band gap of about 3 eV as well as degenerate semiconductor behaviour. The authors hypothesized that the SnO_2 nanoclusters with non-degenerate behaviour consist of Sn^{2+} ions while the degenerate nanoclusters are associated with Sn^{4+} ions. STM–STS investigations [34] of polycrystalline indium tin oxide showed a high degree of mid-gap Fermi level pinning at grain boundaries, in stark contrast to the rest of the sample surface, where the Fermi level was found near the CBM. The surface states responsible for the pinning of the Fermi level were attributed to preferential segregation of surface impurities at grain boundaries, creating a high defect density at boundaries.

The apparent narrowing of the band gap presented in figure 7 could therefore be explained by preferential chemisorption of oxygen species at sintering necks, turning Sn^{2+} lattice ions into Sn^{4+} ions and resulting in a higher density of surface state than at the nanoparticles centres. The UHV anneal prior to scanning might have encouraged migration of adsorbates towards more favourable sites at sintering necks. According to a previous theoretical study [35] on stoichiometric single crystal $SnO_2(110)$ surfaces, the conduction band is mainly derived from the Sn 5s electronic shell while the valence band is mostly related to the O 2p orbitals. High resolution XPS on polycrystalline [36] SnO_2 also showed that the valence band is mainly derived from the O 2p shell. Surface states created by oxygen ions adsorbed on Sn atoms sites are therefore likely to perturb the conduction band derived states and induce surface states within

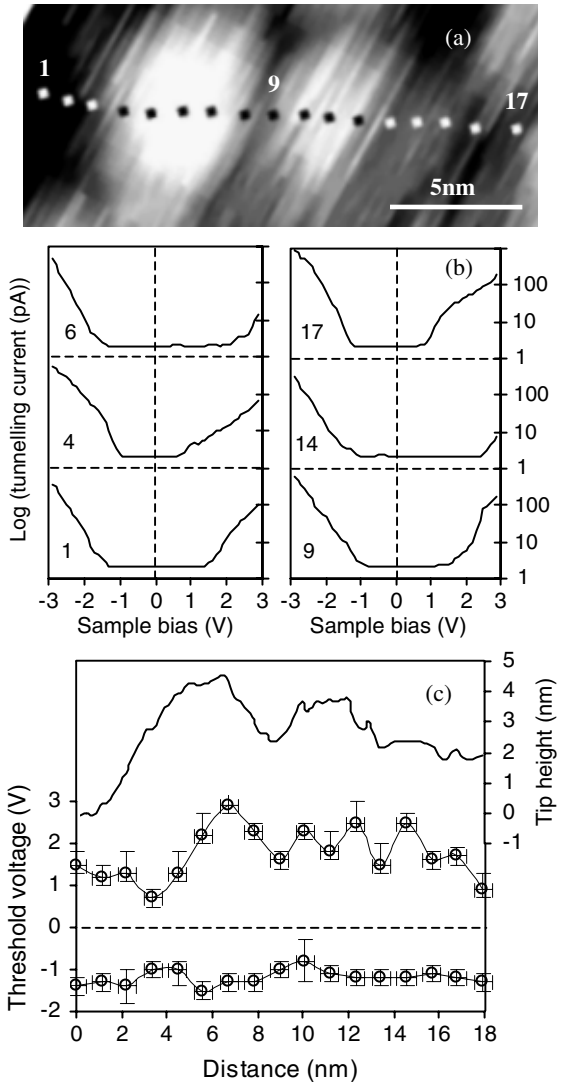

Figure 7. (a) 19 × 8 nm^2 simultaneous STM–STS image of SnO_2 nanocrystals. The numbered (1–17) black and white dots across the nanocrystals show where I–V curves were analysed in order to extract the band edges. (b) A selection of semi-log I–V curves corresponding to STS data points 1, 4, 6, 9, 14 and 17. The curves have been shifted vertically for clarity. (c) Valence band (bottom curve), conduction band (middle curve) and tip height (top curve) profiles across the nanocrystals. The dashed line shows the position of the Fermi level.

the vicinity of the band gap at the CBM. This could explain the fact that the band gap narrowing is mainly due to a decrease of the apparent CBM position with respect to the Fermi level.

Alternatively, the sintering process might have altered the crystallinity of the nanoparticles at the sintering necks, creating defects and rendering the necks amorphous. Highly disordered or amorphous boundaries can result in both acceptor-like and donor-like band gap states [37]. This could also explain the apparent narrowing of the electronic surface band gap at sintering necks. More work is required to clarify the situation, yet the results presented here clearly indicate the power of STM and STS to directly link local electronic properties with nanoscale morphology in a quest to understand and optimize the micro-scale device properties.

4.2. Ni–SiC Schottky barriers

4.2.1. Sample preparations. Samples were made via a number of key stages. Firstly, highly doped n-type SiC substrates with a 10 μm n-type (1×10^{16} cm^{-3}) epilayer were subjected to a solvent clean and a standard RCA etch [38], before the samples were admitted to a high vacuum Edwards deposition chamber. Ni was evaporated from a crucible onto the back of the wafer and annealed in vacuum to 950 °C to form the back Ohmic contact [39]. The sample was then removed and reinserted into vacuum following a further HF etch, with a shadow mask placed over the top of the sample. Ni was evaporated using a well calibrated crystal monitor to yield a thin Ni layer, typically 10–30 nm, deposited at room temperature through the shadow mask present. As a result of the process the sample consisted of an arrangement of faint circular dots of diameter ∼650 μm; these were then individually characterized using a standard I/V measurement. A note was made of each dot's ideality factor and Schottky barrier height, calculated from thermionic emission theory. Typically dots had ideality factors around 1.2–1.3, with barrier heights varying between 1.3 and 1.4 eV. However, if the final processing step included a post-deposition anneal to 450 °C, the I/V characteristic improved drastically and Schottky barrier heights between 1.6 and 1.8 eV were measured [40, 41]. Great care was taken when making contact to the thin Ni Schottky dots to ensure that the I/V probes did not perforate the metal and produce abnormal measurements. The sample was then mounted on a special mini-probe rig, allowing electrical measurements to be made whilst using the SNOM tip. The I/V characteristic of the dot, electrically connected via the mini-probe rig, was always checked to ensure it was consistent with earlier I/V measurements.

In these experiments a commercially available SNOM instrument, the Veeco Aurora II, was used with some minor modifications and additions. Particular care had to be taken to the design of the sample mini-probe rig so that it fitted within the stage of the instrument and did not interfere with instrument optics or SNOM tip. SNOM tips were standard drawn and coated optical fibres and the stage was positioned so as to locate the SNOM tip over the same dot to which electrical contact had been established. In contrast to previous work used to measure photocurrents using SNOM, our measurements used a preamplifier stage connected directly to the sample with a minimum length of shielded cable. This was because even far-field illumination of these contacts only produced small photocurrents when I/V measurements were made. An estimation of the photocurrents produced by nanoscale illumination indicated expected currents in the femto to picoampere range and thus careful design to reduce noise and amplify signals was required. The basis for this was derived from published work [42] on the ballistic electron emission microscopy technique, where small currents are also detected after injection via an STM tip. Figure 8 schematically illustrates the set-up for the experiment, with the incorporation of the chopped laser signal and lock-in-amplifier employed to separate noise from the final signal fed into the control electronics of the SNOM. Using this system and careful selection of scan parameters, chopper frequency and lock-in parameters, it was possible to scan the surface topography and photoresponse simultaneously.

4.2.2. Technical developments for photocurrent measurements. Scans could also be checked for their optical reflectivity over the same sample region and this standard SNOM response checked with the electrical photoresponse over the same region. Reproducibility was checked by observing repeated linescans and this ensured that scanning parameters were suitable and that the tip–sample shear force feedback was appropriate. An example is shown in figure 9, where a 1 μm length is scanned three times and each frame stored. Photoresponse (a) and topography (b) linescans show significant individual reproducibility and comparisons indicate features which are similar on both signals. Also, as each individual line scan can take up to one minute, they demonstrate stability with time. The similarities between both signals may lead

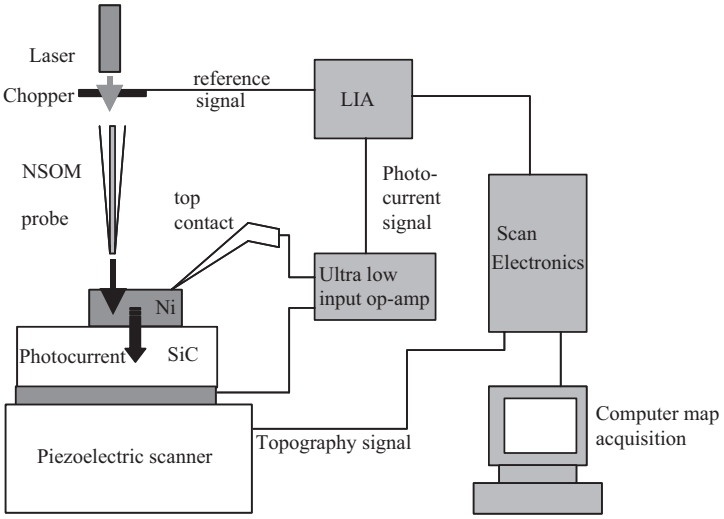

Figure 8. Schematic of the operational set-up for near-field photocurrent measurements.

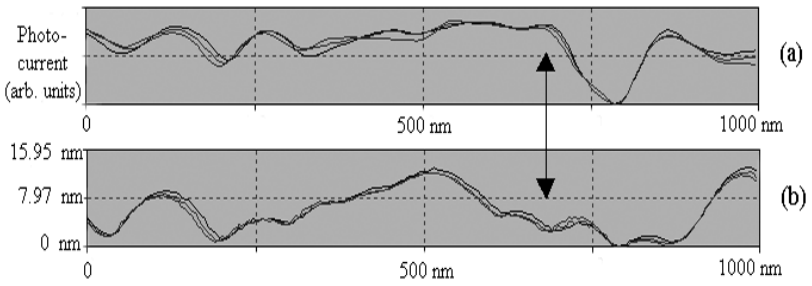

Figure 9. Photocurrent signal (a) and simultaneous topography signal (b), each linescan repeated three times. The arrow indicates significant differences in line profiles.

one to think that the change in topography is ensuring a modification in the photoresponse signal and the possibility of a scanning artefact [22]. However, the linescans indicated features that do not correspond; for instance, the arrow in figure 9 indicates a region where the topography has changed and the photocurrent has remained at a constant level. This can be further verified by measurements made on un-annealed contacts. Figure 10 indicates an area believed to be affected with a residue from solvent rinsing the sample. The large structure seen in the centre of both images (a) and (b) was also seen on many other regions of the diode's surface and also on other diode dots. The black arrow also indicates the edge of another such residue. However, the other features indicated by white arrows were ever present and thought to be raised metal clusters. The key comparison in this image shows that the corresponding photoresponse is positive (white) for the white arrow features (the raised metal clusters) and negative (black) for the residue features (black arrow). The residue feature appears to attenuate the signal from the tip and stop the formation of any photocurrents at the interface. This is also supported by the fact that the photocurrent is responding differently to raised topographic features associated with the Ni surface. Further rinsing and careful drying with nitrogen removed these large residue features when further scans were made, confirming that they were as a result of residue due to the chemical processing of the sample. The black to white scale bar on the photocurrent image is best described as an arbitrary current scale due to dependence of the lock-in amplifier

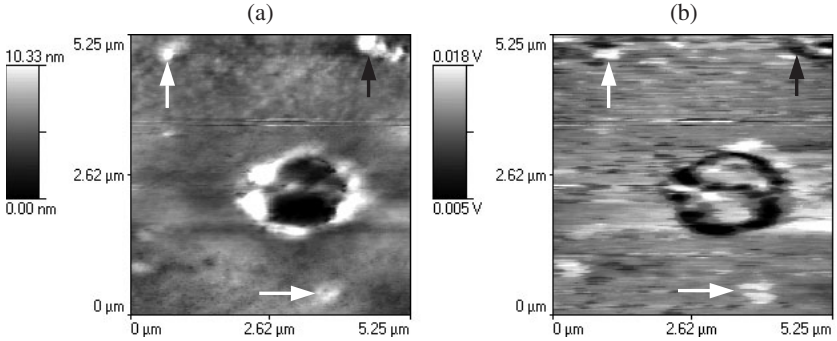

Figure 10. Panel (a) represents a topographic image of an unannealed metal top-contact; the large feature shows a raised topography. Panel (b) represents a photocurrent image of the same region, showing a similar large feature but with the photocurrent reduced. The arrows indicate other areas of comparison which are discussed in the text.

voltage output, and ultimately the intensity of the near-field source and magnitude of the generated photocurrent.

Figure 10 also indicates a positive response to a persistent problem associated with using the near-field techniques, namely scanning artefacts [22]. Changes in SNOM tip–sample distance can greatly affect the coupling of the near-field and hence the subsequent optical response of the sample. In figure 10 it is clear that an increase (or decrease) in topography did not always produce the same direction of change in the photocurrent signal. If this had been the case it would have been likely to be due to variations in the near field signal. As mentioned in the earlier section concerning the SNOM technique, repeating the scan with different feedback parameters also helped to ensure that artefacts could be distinguished. Differences in the topography and photocurrent response indicate a clear mechanism affecting the generation of a photocurrent and possible variation in sample properties in these regions. This can be further verified when scanning different samples and also scanning identical regions with different laser wavelengths. In these experiments two laser sources, Ar ion (green, ∼2.55 eV) and HeNe (red, ∼1.9 eV), have been used to further elucidate changes seen in photocurrent response.

4.2.3. Annealed and unannealed contacts: surface morphology. The mechanism which produced the variation in barrier height in response to the annealing temperature of the Ni contacts is of great interest, and the thin Ni surface topography was an important characteristic to quantify. Figure 11 shows two topographic images of Ni contacts made using the shear force microscopy mode of the SNOM. It is clear that the surface structure of the two samples has changed drastically as a result of their preparation. Panel (a) is a contact which has been annealed to 450 °C, whereas (b) has been produced at room temperature (RT). Clearly the cluster size of the Ni has altered and the surface black–white ratio has increased drastically from ∼5 to 21 nm as a result of annealing. As mentioned earlier, this annealing process leads to the increase in Schottky barrier height and the mechanism is likely to be associated with the interface chemistry and defects present at the interface [41]. These images indicate that this electrical modification has been accompanied by significant changes in the surface morphology of the contact. Further analysis of these images revealed that the average surface roughness of the annealed sample was ∼3.2 nm compared with the unannealed (RT) average surface roughness of ∼0.7 nm. Average surface roughness is a measure of the arithmetic mean of the deviations in the height from the mean height value for every point in the image. To ensure that possible variations in the overall thickness of the Ni layer were not dominating this result, a large number of samples were scanned and variations in the layer thickness examined. The

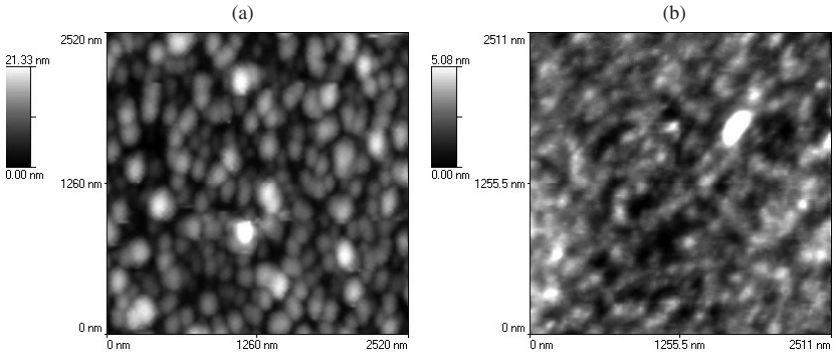

Figure 11. Topographic images of an Ni contact (a) annealed to 450 °C, (b) grown at RT.

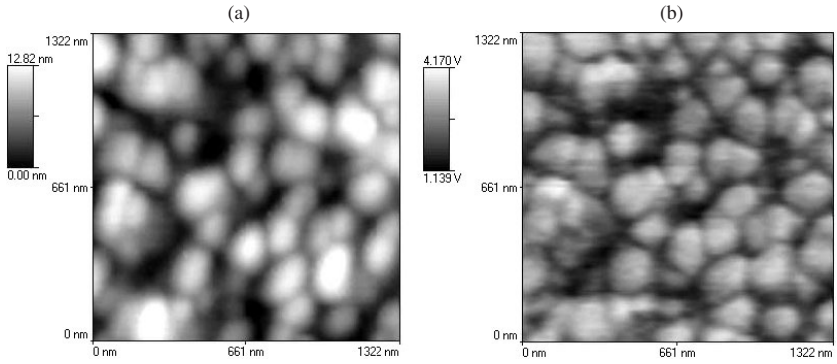

Figure 12. Two simultaneous images of a 1.322 μm^2 area on an annealed Ni top contact on SiC where (a) represents the topography and (b) represents the photocurrent image produced with a red laser. The same homogeneous contrast is seen with the green laser. Within the grains no variation in photocurrent is seen regardless of the grain thickness.

clustering at elevated temperatures was found to be independent of layer thickness and was also seen to occur when RT samples were readmitted into vacuum and annealed. Variations in anneal temperature also altered the final cluster size and distribution. Subsequently this has also been observed on UHV prepared samples.

4.2.4. Photocurrent measurements from annealed Ni contacts. Scanning annealed contacts with the larger barriers of ∼1.8 eV was experimentally more suitable to the set-up due to the energy of the two laser wavelengths available (equivalent to 1.9 and 2.55 eV). Thus any regions scanned which had a barrier larger than 1.9 eV may then be differentiated with two images sampled at these wavelengths. In figures 12(a) and (b) are typical simultaneous images from the annealed top Ni contact, showing topography and photocurrent signals respectively. To generate the photocurrent image, the HeNe laser source was used with a wavelength of 632.8 nm (∼1.9 eV). It is clear from this figure that the features seen in topography are, in the main, mirrored in the photocurrent image. The resolutions are also very much compatible on this scale. Cross-sections (not shown here) indicated that the photocurrent response was very rapid across features, as though it was being switched on and off abruptly. The photocurrent image is also seen to be very uniform in contrast, with clusters all indicating a similar maximum response. This is distinctly different from the topography as this varied gradually over the clusters. Moreover, clusters had a variety of maximum heights. This would indicate

that although the topography is constantly changing within a single cluster, the photocurrent response is largely unaffected by scanning. This was seen to be repeatable with alternative scan parameters, where feedback and scan speed were altered. However, as the tip scans the entire surface, from cluster to cluster, the roughness of the sample is likely to lead to a change in the tip–sample distance and thus the coupled intensity of the near-field light into the sample. Hence abrupt changes in the photocurrent between clusters could be as a result of the intensity of light as opposed to a change in Schottky barrier inhibiting the measured photocurrent. There is another possibility: that these regions between clusters actually represent voids generated in the thin layer and the photocurrent is not being generated due to the absence of metal. This was examined by scanning the edge of the contact, but very often those regions were graded, with some samples showing clusters on the substrate and others clusters superimposed on thin metal layers. Measurements were also made on the same region using the green Ar ion laser. The photocurrent image appeared almost identical to figure 12(b) taken with the HeNe laser, indicating that the two wavelengths do not show significant differences in the electrical nature of the surface as a function of energy between 1.9 and 2.55 eV. Further evidence is required to ascertain whether the effect is due to the absence of metal and voids or the near-field.

5. Conclusions

In this paper we have demonstrated how scanning probe techniques can be used to correlate surface electronic properties with the local morphology of electronic devices where surface (or interface) features on the nanometre scale play a crucial role in device performances. We used STM–STS to study real nanocrystalline SnO_2 gas sensors and SNOM to investigate Ni–SiC Schottky diodes. For SnO_2 gas sensors, STM imaging showed the effect of sintering on the morphology of SnO_2 films made with 8 nm SnO_2 powder, and confirmed the optimum sintering temperature of 400 °C. Annealing at temperatures of 450 and 500 °C resulted in extensive merging of the nanoparticles, detrimental to gas sensing performances. Simultaneous STM–STS measurements showed a correlation between the topography of sintered nanoparticles and their surface electronic properties. The STS measured surface band gap appeared to shrink at sintering necks. Surface states created by the preferential chemisorption of oxygen species at sintering necks have been put forward as a possible interpretation. A modified SNOM set-up was used to simultaneously acquire topography and photocurrent maps of thin (10–30 nm) Ni–SiC contacts before and after annealing at 450 °C. From our studies it is clear that annealing the samples to 450 °C has a profound affect on the surface topography of the Ni contacts, and this is accompanied by a change in Schottky barrier of the contact. The morphology indicates nanometre-sized clusters of Ni, with a large void density. This is in agreement with TEM measurements made by Pécz [41], where Ni clustering and voids were seen upon annealing contacts to 950 °C. Using SNOM it was possible to achieve localised submicron photocurrent measurements from annealed contacts. Photocurrent images indicated responses mostly characteristic of the surface topography, and artefacts are discussed as a possible cause. Regions where photocurrent response was independent of the topography have also been isolated and changes in localised Schottky barrier height discussed. Regions with no photocurrent signal were correlated to voids, and the photoresponse of individual clusters was seen not to change significantly with the varying cluster topography, indicating independence between the two. In addition features that were dependant on wavelength were also evident and require further investigation, whereupon applying a sample bias will also be examined. It is suspected that these characteristics may be as a result of lateral variations of the recombination rate or of metal thickness [43]. Examination of the more suitable, flatter unannealed contacts is likely to reduce the possibility of artefacts. Furthermore, coupling the

SNOM to a tunable laser source, which is tuned to the appropriate Schottky barrier height energy, will provide a more quantitative measurement of inhomogeneity on such contacts. This detailed study will be the subject of a separate publication by the authors.

References

[1] Ihokura K, Tanaka K and Murakami N 1983 *Sensors Actuators* **4** 607
[2] Wada K and Egashira M 2000 *Sensors Actuators* B **62** 211
[3] Martinelli G, Carotta M C, Traversa E and Ghiotti G 1999 *MRS Bull* **24** 30
[4] Hallin C, Yakimova R, Pécz B, Georgieva A, Marinova T S, Kasamakova L, Kakanakov R and Janzén E 1997 *J. Electron. Mater.* **26** 119
[5] Sieber N, Mantel B F, Seyller T, Ristein J, Ley L, Heller T, Batchelor D R and Schmeisser D 2001 *Appl. Phys. Lett.* **78** 1216
[6] Almeida J, Tiziana dell'Orto, Coluzza C, Margaritondo G, Bergossi O, Spajer M and Courjon D 1996 *Appl. Phys. Lett.* **69** 2361
[7] Hallen H D, La Rosa A H and Jahncke C L 1995 *Phys. Status Solidi* a **152** 257
[8] Hsu J W P 2001 *Mater. Sci. Eng.* **33** 1
[9] Wilks S P, Teng K S, Dunstan P R and Williams R H 2002 *Appl. Surf. Sci.* **190** 467
[10] Stroscio J A and Kaiser W J (ed) 1993 *Scanning Tunnelling Microscopy* (New York: Academic)
[11] Hammers R J, Trump R M and Demuth J E 1986 *Phys. Rev. Lett.* **56** 1972
[12] Feenstra R M, Stroscio J A and Fein A P 1987 *Surf. Sci.* **181** 295
[13] Pohl D W 1984 *Appl. Phys. Lett.* **44** 1
[14] Synge E H 1928 *Phil. Mag.* **6** 356
[15] Karrai K and Grober R 1995 *Appl. Phys. Lett.* **66** 1842
[16] Paesler M A and Moyer P J 1996 *Near Field Optics: Theory, Instrumentation, and Applications* (New York: Wiley)
[17] Pohl D W 1993 *Near Field Optics* ed D W Pohl and D Courjon (Dordrecht: Kluwer)
[18] Gao H, Oberringer M, Englisch A, Hanselmann R G and Hartmann U 2001 *Ultramicroscopy* **86** 145
[19] Coluzza C, Almeida J, Tiziana dell'Orto, Barbo F, Bertolo M, Bianco A, Cerasari S, Bergossi O, Spajer M and Courjon D 1996 *Appl. Surf. Sci.* **104/105** 196
[20] Unlu M S, Goldberg B B, Herzog W D, Sun D and Towe E 1995 *Appl. Phys. Lett.* **67** 1862
[21] Cramer R M, Schade W R, Heiderhoff R, Balk L J and Chin R 1998 *Microelectron. Reliab.* **38** 963
[22] Hecht B, Bielefeldt H, Inouye Y, Pohl D and Novotny L 1997 *Appl. Phys.* **81** 2492
[23] Williamson R L, Brereton L J, Antognozzi M and Miles M J 1998 *Ultramicroscopy* **71** 165
[24] Coluzza C, Di Claudio G, Davy S, Spajer M, Courjon D, Cricenti A, Generosi R, Faini G J, Almeida J, Conforto E and Margaritondo G 1999 *J. Microsc.* **194** 401
[25] Kaiser W J, Bell L D and 1988 *Phys. Rev. Lett.* **60** 1406
[26] Fowell A E, Williams R H, Richardson B E, Cafolla A A, Westwood D I and Woolf D A 1991 *J. Vac. Sci. Technol.* B **9** 581
[27] Roy Morrison R 1982 *Sensors Actuators* **2** 329
[28] Schierbaum K D, Weimar U, Göpel W and Kowalkowski R 1991 *Sensors Actuators* B **3** 205–14
[29] Naser J, Ferkel H, Riehemann W and Mordike B L 1999 *Lasers Eng.* **9** 195
[30] Feenstra R M 1994 *Phys. Rev.* B **50** 4561
[31] Arbiol J, Gorostiza P, Cicera A, Cornet A and Morantes J 2001 *Sensors Actuators* B **78** 57–63
[32] Romppainen P and Lantto V 1988 *J. Appl. Phys.* **63** 5159
[33] Kaplan L, Rusman I, Boxman R L, Goldsmith S, Nathan M and Ben-Jacob E 1996 *Thin Solid Films* **290/291** 355–61
[34] Kasiviswanathan S, Srinivas V, Kar A K, Mathur B K and Chopra K L 1997 *Solid State Commun.* **101** 831–4
[35] Rantala T T, Rantala T S and Lantto V 2000 *Mater. Sci. Semicond. Process.* **3** 103–7
[36] Köver L, Kovács Zs, Sanjinés R, Moretti G, Cserny I, Margaritondo G, Pálinkas J and Adachi H 1995 *Surf. Interface Anal.* **23** 461–6
[37] Mott N F and Davis E A 1979 *Electronic Processes in Non-Crystalline Materials* (Oxford: Clarendon)
[38] Kern W and Puotinen D A 1970 *RCA Rev.* **31** 187
[39] Lui S, Reinhardt K, Severt C and Scofield J 1996 *Institute of Physics Conference Series* No 142 (*Silicon Carbide and Related Materials 1995: Proc. 6th International Conf.*) p 677
[40] Kestle A, Dunstan P R, Wilks S P, Pritchard M and Mawby P A 2000 *Electron. Lett.* **36** 267
[41] Pécz B 2001 *Appl. Surf. Sci.* **7481** 1–8
[42] Gangopadhyay S, Kar A K, Ray S K and Mathur B K 2000 *Appl. Surf. Sci.* **156** 183
[43] Almeida J, Margaritondo G, Coluzza C, Davy S, Spajer M and Courjon D 1998 *Appl. Surf. Sci.* **125** 6–10